optica

Megahertz x-ray microscopy at x-ray free-electron laser and synchrotron sources: supplementary material

PATRIK VAGOVIČ,[1,2,3,*] TOKUSHI SATO,[1,2] LADISLAV MIKEŠ,[2] GRANT MILLS,[2] RITA GRACEFFA,[2] FRANS MATTSSON,[4] PABLO VILLANUEVA-PEREZ,[4,1] ALEXEY ERSHOV,[5] TOMÁŠ FARAGÓ,[5] JOZEF ULIČNÝ,[6] HENRY KIRKWOOD,[2] ROMAIN LETRUN,[2] RAJMUND MOKSO,[4] MARIE-CHRISTINE ZDORA,[7,8,9] MARGIE P. OLBINADO,[10] ALEXANDER RACK,[10] TILO BAUMBACH,[5] JOACHIM SCHULZ,[2] ALKE MEENTS,[1] HENRY N. CHAPMAN,[1] AND ADRIAN P. MANCUSO[2,11]

[1]*Center for Free-Electron Laser, Notkestraße 85, 22607 Hamburg, Germany*
[2]*European XFEL, Holzkoppel 4, 22869 Schenefeld, Germany*
[3]*Institute of Physics, Academy of Sciences of the Czech Republic v.v.i., Na Slovance 2, 182 21, Praha 8, Czech Republic*
[4]*Lund University, Sweden*
[5]*Institute for Photon Science and Synchrotron Radiation, Karlsruhe Institute of Technology (KIT), Herrmann-von-Helmholtz-Platz 1, 76344 Eggenstein-Leopoldshafen, Germany*
[6]*Faculty of Science, Department of Biophysics, P. J. Šafárik University, Jesenná 5, 04154 Košice, Slovakia*
[7]*Diamond Light Source, Harwell Science and Innovation Campus, Didcot, Oxfordshire OX11 0DE, UK*
[8]*Department of Physics & Astronomy, University College London, London, WC1E 6BT, UK*
[9]*Department of Physics & Astronomy, University of Southampton, Southampton SO17 1BJ, UK*
[10]*ESRF – The European Synchrotron, 71 Avenue des Martyrs, 38000 Grenoble, France*
[11]*Department of Chemistry and Physics, La Trobe Institute for Molecular Science, La Trobe University, Melbourne, Victoria 3086, Australia*
Corresponding author: patrik.vagovic@xfel.eu

Published 23 August 2019

This document provides supplementary material to "Megahertz x-ray microscopy at x-ray free-electron laser and synchrotron sources," https://doi.org/10.1364/OPTICA.6.001106. We describe both experimental setups in detail and quantitative image comparison.

1. EXPERIMENTAL DESCRIPTION

For the experiment at EuXFEL we used the SPB/SFX instrument [1]. For the X-ray microscopy measurements, we re-used the spent beam from the upstream interaction region that had passed through the central hole of an AGIPD detector [2] and was out-coupled into air via a 180 µm thick diamond window. A simultaneous crystallography experiment and timing measurement using a photon arrival monitor [3] was performed during MHz X-ray imaging. The beam from the SASE1 undulator source was delivered by the horizontal offset mirrors placed 260 m downstream of the source [4]. KB mirrors installed in the optics hutch [5] were used to focus the beam into the sample chamber with a focal spot size of 3 µm × 3 µm. The focus-to-detector distance was 7.2 m, the sample-to-detector distance was 0.29 m and the total air path between the diamond window and the detector was 0.96 m. The optical configuration is depicted on Fig. 1.

A photon energy of 9.3 keV was used and the pulse train was filled with 128 X-ray pulses with a repetition rate of 1.128 MHz. The 10× magnification by the diffraction-limited microscope coupled to the 8 µm thick LYSO:Ce sctintillator resulted in an effective pixel size of 3.2 µm and a FOV of 1.28 mm × 0.8 mm. The Mitutoyo near-ultraviolet wavelength corrected M Plan Apo infinity corrected objective with numerical aperture 0.28 was coupled with Mitutoyo MT-L 200 mm tube lens. The spatial resolution of this imaging system was therefore limited by the

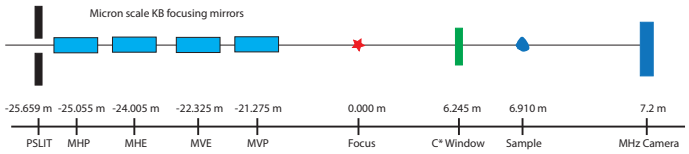

Fig. 1. Optical configuration for MHz imaging at EuXFEL SPB/SFX instrument.

effective pixel size of the FT-CMOS camera Shimadzu HPV-X2. The X-ray pulse energy measured with a gas detection monitor at the end of the SASE 1 tunnel was about 750 µJ. The sample position in the interaction region of the X-ray and visible light lasers were locked optically using two high-resolution optical microscopes. The timing alignment was performed using temporal position of the scattered radiation of the X-ray and visible laser pulses from the scattering material placed at the sample position measured using a fast silicon diode connected to oscilloscope (LeCroy WaveRunner 8404M). The time alignment of the visible light pump laser with X-ray pump laser was done by shifting the synchronized 10Hz train signal, which indicates the start of each pulse train by a delay generator (Stanford Research DG645).

As a sample we used a glass capillary with internal diameter of 300 µm and wall thickness of 25 µm. The capillary was filled with purified water and supplied via a remotely controlled syringe pump.

For the experiment at the ESRF synchrotron we used the 16-bunch filling mode [6] providing a bunch separation of 176 ns and the MHz camera was recording every third frame with an inter-frame time of 530 ns. The harmonics of the undulator with central photon energy 32 keV were conditioned by a set of ten Beryllium compound refractive lenses with radius of curvature 0.5 mm and aperture of 1.3 mm focusing in vertical plane to enhance the flux density at the detector. The fast camera was coupled to the microscope with 4× magnification, 0.2 numerical aperture and 250 µm thick LYSO:Ce scintillator providing an effective pixel size of 8 µm and a FOV of 2.0 mm × 3.0 mm. The sample-to-detector distance was 1 m. As a sample we used a glass capillary with internal diameter of 500 µm and wall thickness of 270 µm. Purified water was mixed with Nile blue dye to enhance absorption of laser power in the water. A pulsed Nd:YAG laser (Minilite II, Continuum) was used to generate the water jet by power absorption in the water. The laser wavelength was 532 nm with a pulse duration 3-5 ns, and the attenuated laser beam energy was 2.03 mJ with a focal spot size of 300 µm. The 10 Hz laser flash lamp and Q-switch operation were synchronized with the RF system using the BCDU8 unit and a delay generator (DG 645, Stanford Instruments). Experimental arrangement for EuXFEL is shown in Fig. 2 and for ESRF setup in Fig. 3.

2. IMAGE FLOW ANALYSIS

In this section we describe the procedure for the optical flow analysis shown in the main paper. To remove normalization artifacts and high frequency noise for the EuXFEL data we performed an adaptive high pass filtering by subtracting a low-pass filtered (Gaussian convolution with the standard deviation σ = 5 pixels) image from its original version. This procedure significantly suppressed spatio-temporal image flickering. Using such image processing, we visualized the velocities of breaking glass reaching 35 m/s using flow analysis based on variational optical flow methods [7]. Such methods combine a data term that imposes constraints on image brightness and a smoothness term which regulates the properties of the flow field. A global model containing both constraints is then minimized to find a solution. Relying on spatial image gradients, the optical flow cannot be uniquely computed within homogeneous image regions. Thus the "edge enhancement" contrast which highlights sharp object boundaries is beneficial for the optical flow under the assumption of small displacements. The computed velocities provide quantitative information about complex kinematics of the burst process.

3. IMAGE QUALITY COMPARISON

To compare quantitatively the image quality between the two experiments, first the signal-to-noise ratio (SNR) was evaluated. Figures 4 and 5 show the results and frames used for the comparison. For each sequence frames with the sample were used and normalized by the frames without the sample. The SNR for each frame in the sequence was calculated by division of the mean values of normalized area containing the signal of the sample C_c by the standard deviation of the normalized area B_c without the sample. As can be clearly seen from the distribution of the mean values (Fig.4d and Fig.5d) the pulse-to-pulse intensity fluctuations are strong in case of EuXFEL, which is due to the origin of the photons generation at XFELs using self-amplified spontaneous emission (SASE). Pointing fluctuations are pronounced at EuXFEL, as at all SASE XFELs. Modal composition of the spectrum and pulse-to-pulse energy fluctuations result in pulse-to-pulse wave front variations [8]. All such instabilities contribute to the measured image intensity distribution, which in turn varies from pulse to pulse.

This makes it difficult to perform a standard normalization of image frames by the background frame and it leads to the fluctuation of the standard deviation. Such fluctuations at the synchrotron are much smaller as it is clearly seen from the mean values in Fig. 5. Another source of standard deviation increase in case of the EuXFEL data is the strong high-frequency noise caused by the beam delivery KB optics manifested as vertical and horizontal stripes. This can be in future improved by better illumination, for example by using direct beam illumination. The longer-period oscillations in mean values in Fig. 5 are present due to the not exact synchronization of the camera to the master frequency of the X-ray pulses as the camera clock has a different frequency. Such oscillations are present as well in the EuXFEL data but with much smaller period resulting in only little or no illumination of certain frames in the sequence.

By comparing the SNR of the two data sets, we can conclude that the EuXFEL data have a clearly higher SNR by almost a factor of two. The results from the EuXFEL also indicate that despite using a much less efficient imaging system and a higher magnification, a stronger signal is detected. This performance can unlock fast dynamics at even higher spatial resolution. However, due to the very different experimental conditions (different photon energy, magnification, scintillator thickness, optics efficiency) such comparison is not entirely correct. A more objective comparison can be achieved by looking at the power spectrum. For this purpose we selected the frames with the highest SNR for both the ESRF and the EuXFEL data and calculated the power spectrum from normalized areas A_c from both data sets. Using a Fourier transform, we calculated the power of the corresponding frames as

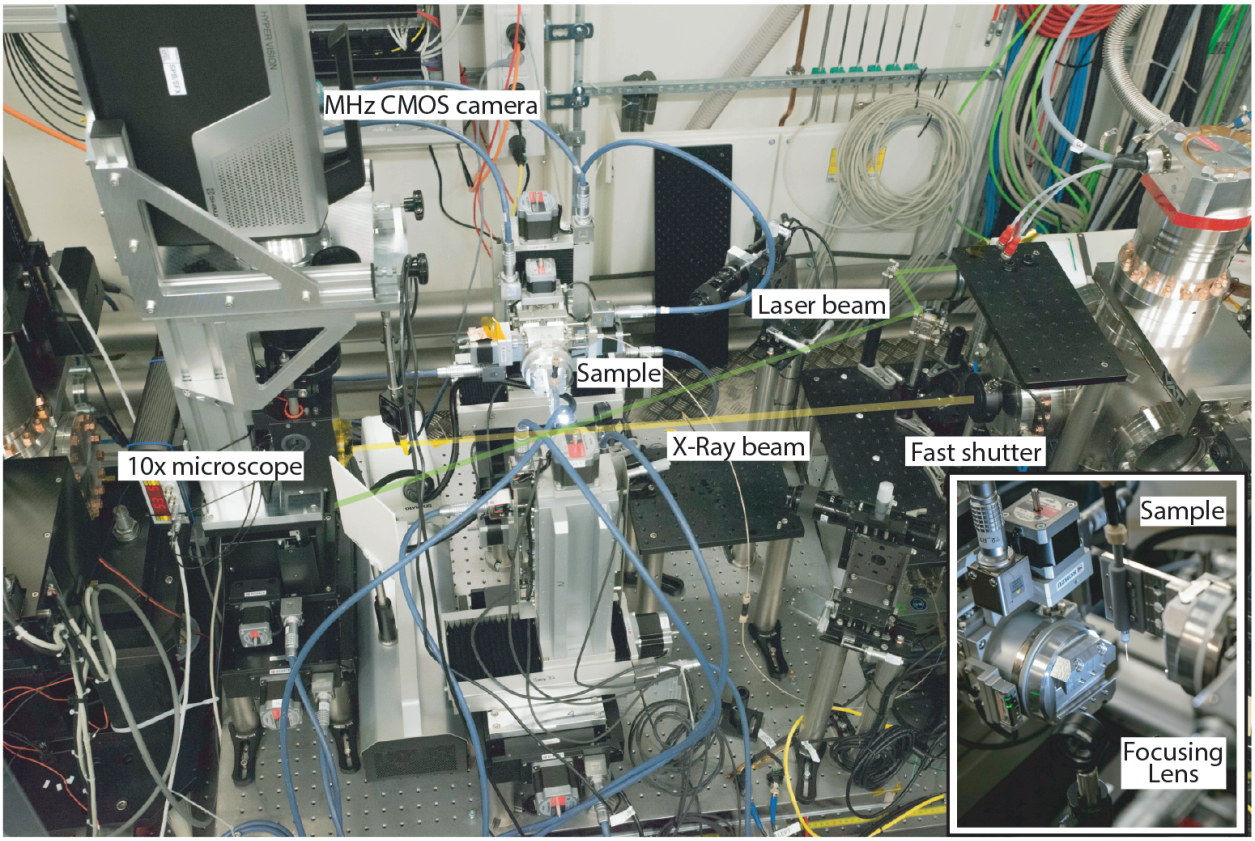

Fig. 2. Experimental setup for MHz microscopy at EuXFEL SPB/SFX instrument.

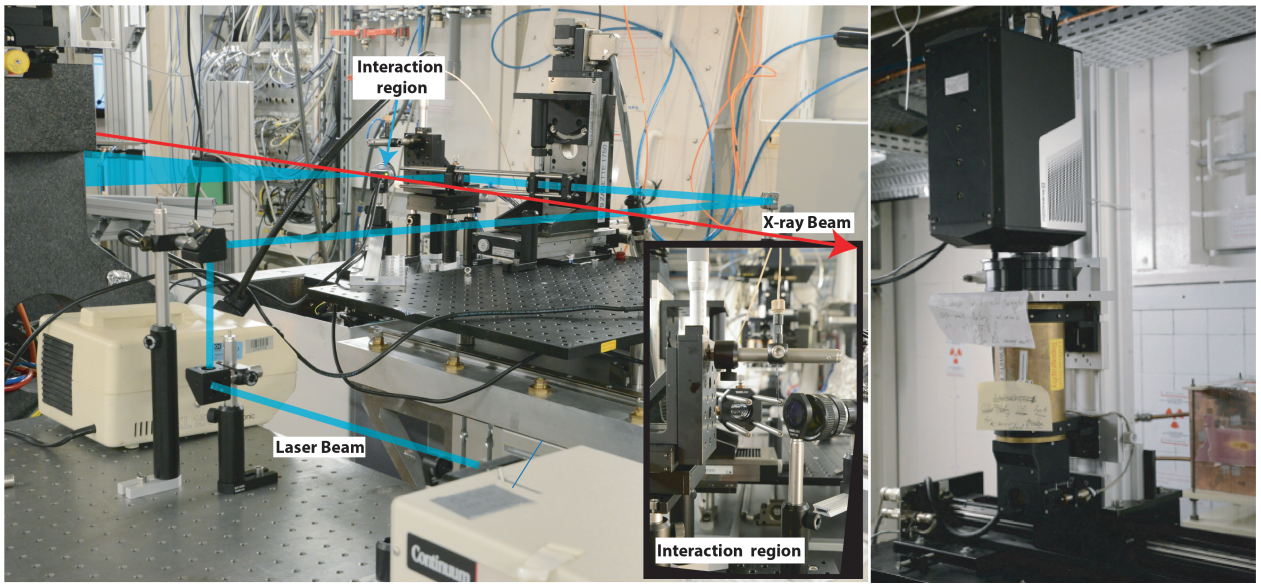

Fig. 3. Experimental setup for MHz microscopy at ESRF ID19 beamline.

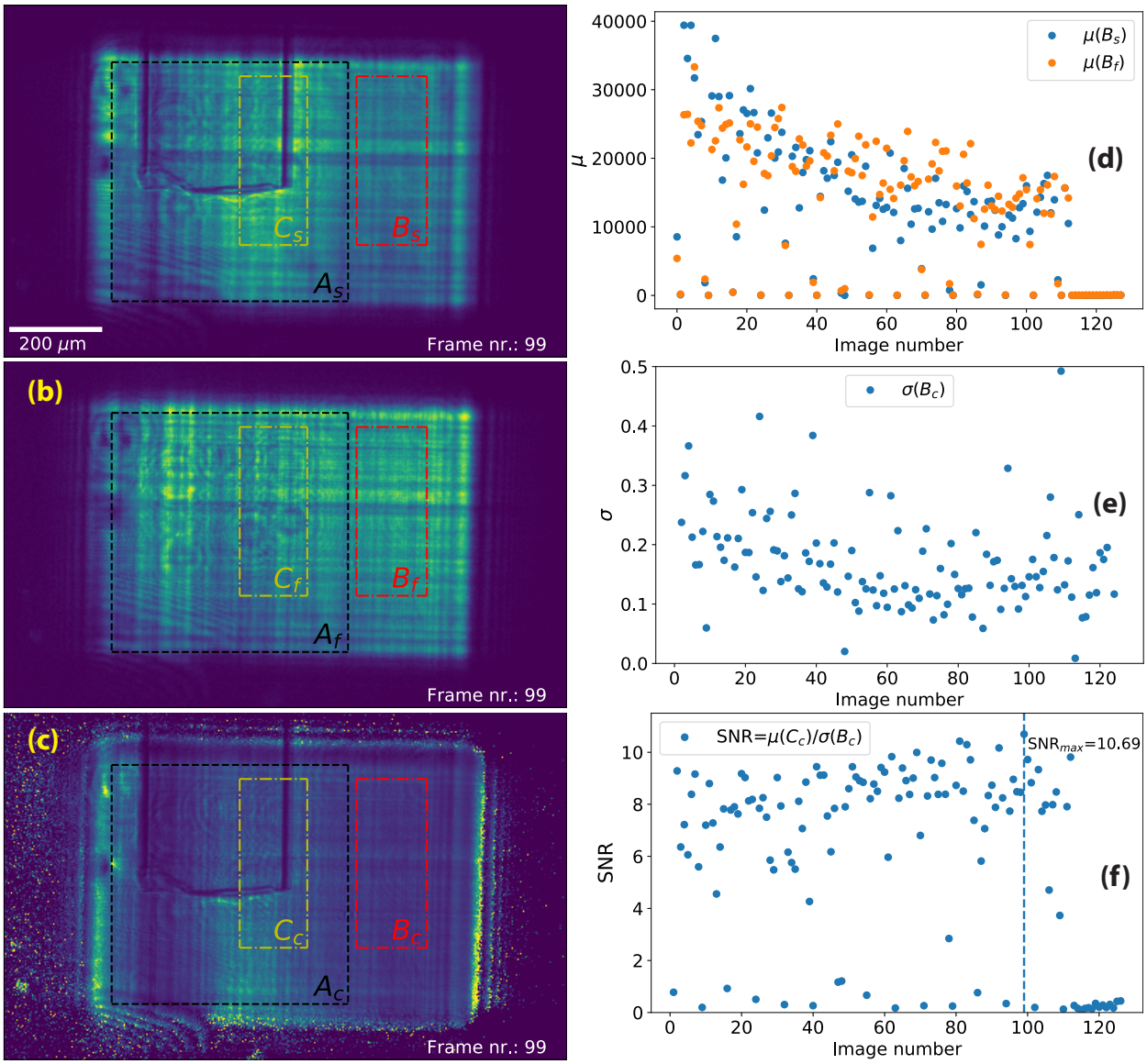

Fig. 4. SNR comparison on a static sample using EuXFEL data. Signal evaluation was done by looking at the raw sequences with sample (a) and without sample (b) using the areas marked in the figures ($B_{s,f,c}$ and $C_{s,f,c}$), where the subscripts indicate: s - sequence with sample, f - flat sequence without sample and c - corrected sequence. Area A_c was used to evaluate the power spectrum. Figure (d) shows the mean values for areas B_s and B_f over the image sequence revealing strong pulse-to-pulse intensity fluctuations. The standard deviation was evaluated on the background corrected area B_c and finally the SNR showing a maximum of 10.69 was calculated by division of mean values (d) by standard deviation values (e) for a given frame in the sequence.

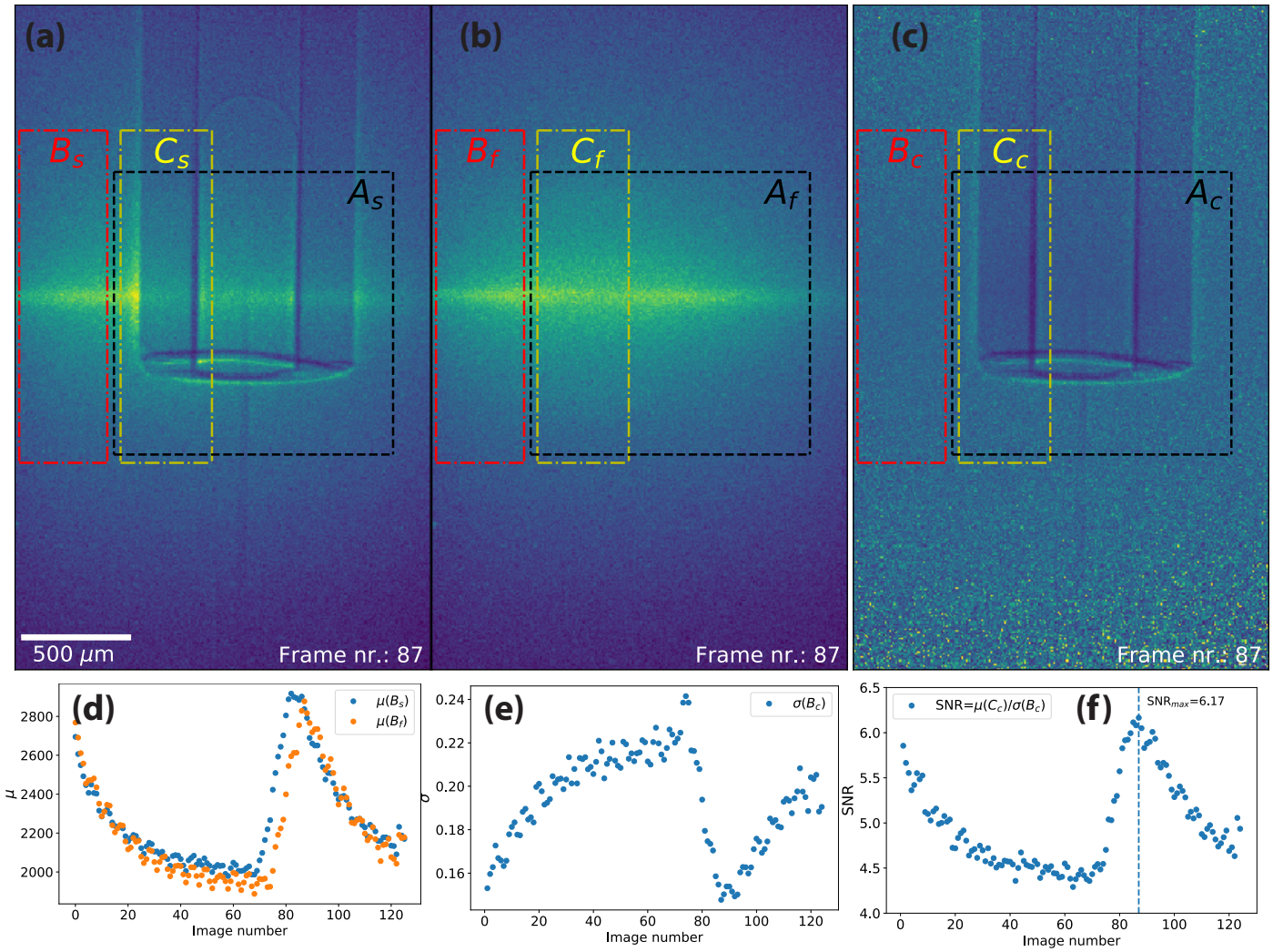

Fig. 5. SNR comparison on a static sample using ESRF data. Signal evaluation was done by using the raw sequences with sample (a) and without sample (b) looking at the areas marked in the figures ($B_{s,f,c}$ and $C_{s,f,c}$). Area A_c was to evaluate power spectrum. Figure (d) shows the mean values for areas B_s and B_f over the image sequence. The standard deviation was evaluated on the background corrected area B_c and finally standard deviation showing maximum of 6.17 was calculated by division of mean values (d) by standard deviation values (e) for given frame in the sequence.

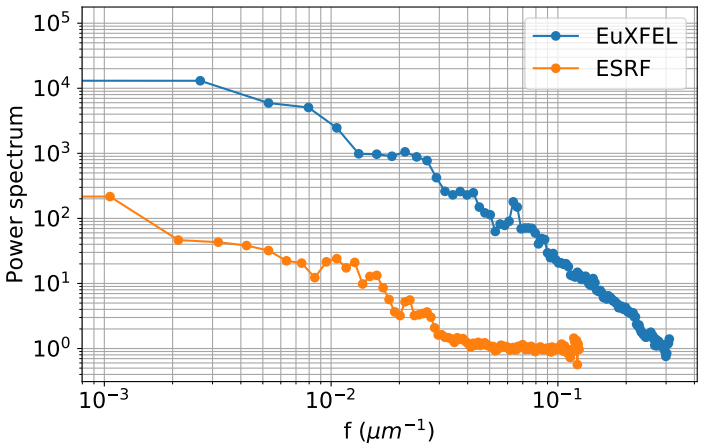

Fig. 6. Power spectra of the frames with the highest SNR for the XFEL (SNR = 10.69) and the ESRF (SNR = 6.17) data. Power spectra were calculated from the normalized frames using areas A_c depicted in figures 4 and 5.

$$P(k_x, k_y) = |FFT(A_c(x, y))|^2 \quad (1)$$

and then integrated the spectrum in polar coordinates. The resulting graphs are shown in Fig. 6. The EuXFEL power spectrum is superior over the ESRF power spectrum as it is higher by one to almost two orders of magnitude over the entire range of spatial frequencies.

REFERENCES

1. A. P. Mancuso, A. Aquila, L. Batchelor, R. J. Bean, J. Bielecki, G. Borchers, K. Doerner, K. Giewekemeyer, R. Graceffa, O. D. Kelsey, Y. Kim, H. J. Kirkwood, A. Legrand, R. Letrun, B. Manning, L. Lopez Morillo, M. Messerschmidt, G. Mills, S. Raabe, N. Reimers, A. Round, T. Sato, J. Schulz, C. Signe Takem, M. Sikorski, S. Stern, P. Thute, P. Vagovič, B. Weinhausen, and T. Tschentscher, "The Single Particles, Clusters and Biomolecules and Serial Femtosecond Crystallography instrument of the European XFEL: initial installation," J. Synchrotron Radiat. **26**, 660–676 (2019).
2. J. Schwandt, E. Fretwurst, R. Klanner, and J. Zhang, "Design of the AGIPD sensor for the european XFEL," J. Instrumentation **8**, C01015–C01015 (2013).
3. H. J. Kirkwood, R. Letrun, T. Tanikawa, J. Liu, M. Nakatsutsumi, M. Emons, T. Jezynski, G. Palmer, M. Lederer, R. Bean, J. Buck, S. D. D. Cafisio, R. Graceffa, J. Grünert, S. Göde, H. Höppner, Y. Kim, Z. Konopkova, G. Mills, M. Makita, A. Pelka, T. R. Preston, M. Sikorski, C. M. S. Takem, K. Giewekemeyer, M. Chollet, P. Vagovic, H. N. Chapman, A. P. Mancuso, and T. Sato, "Initial observations of the femtosecond timing jitter at the european xfel," Opt. Lett. **44**, 1650–1653 (2019).
4. H. Sinn, M. Dommach, B. Dickert, M. Di Felice, X. Dong, J. Eidam, D. Finze, I. Freijo-Martin, N. Gerasimova, N. Kohlstrunk, D. La Civita, F. Meyn, V. Music, M. Neumann, M. Petrich, B. Rio, L. Samoylova, S. Schmidtchen, M. Störmer, A. Trapp, M. Vannoni, R. Villanueva, and F. Yang, "The SASE1 X-ray beam transport system," J. Synchrotron Radiat. **26**, 692–699 (2019).
5. R. J. Bean, A. Aquila, L. Samoylova, and A. P. Mancuso, "Design of the mirror optical systems for coherent diffractive imaging at the SPB/SFX instrument of the european XFEL," J. Opt. **18**, 074011 (2016).
6. "ESRF Filling Modes," http://www.esrf.eu/Accelerators/Operation/Modes.
7. A. Myagotin, A. Ershov, L. Helfen, R. Verdejo, A. Belyaev, and T. Baumbach, "Coalescence analysis for evolving foams via optical flow computation on projection image sequences," J Synchrotron Radiat **19**, 483–491 (2012).
8. M. Seaberg, R. Cojocaru, S. Berujon, E. Ziegler, A. Jaggi, J. Krempasky, F. Seiboth, A. Aquila, Y. Liu, A. Sakdinawat, H. J. Lee, U. Flechsig, L. Patthey, F. Koch, G. Seniutinas, C. David, D. Zhu, L. Mikeš, M. Makita, T. Koyama, A. P. Mancuso, H. N. Chapman, and P. Vagovič, "Wavefront sensing at X-ray free-electron lasers," J. Synchrotron Radiat. **26**, 1115–1126 (2019).